Rapid Communications

Electrically controlled switching of the magnetization state in multiferroic $BaTiO_3$/CoFe submicrometer structures

R. Lo Conte,[1,*] J. Gorchon,[1,2] A. Mougin,[3] C. H. A. Lambert,[1] A. El-Ghazaly,[1] A. Scholl,[4] S. Salahuddin,[1] and J. Bokor[1,2,†]

[1]*Department of Electrical Engineering and Computer Science, University of California, Berkeley, California 94720, USA*

[2]*Materials Sciences Division, Lawrence Berkeley National Laboratory, Berkeley, California 94720, USA*

[3]*Laboratoire de Physique des Solides, CNRS, Université Paris-Sud, Université Paris-Saclay, 91405 Orsay Cedex, France*

[4]*Advanced Light Source, Lawrence Berkeley National Laboratory, Berkeley, California 94720, USA*

(Received 11 May 2018; revised manuscript received 9 July 2018; published 5 September 2018)

The development of reliable and highly energy efficient multiferroic nanosystems, which can function at room temperature, is key for the design of ultralow-power magnetoelectric devices. Here, we report electrically controlled magnetic domain wall motion and magnetization switching in $BaTiO_3/Co_{50}Fe_{50}$ microstructures, at room temperature. The perfect one-to-one connection between the ferroelectric domain pattern of the $BaTiO_3$ crystal and the ferromagnetic state of the CoFe microstructures, which relies on a strain-induced magnetic anisotropy modification, is the cause of the observed magnetoelectric effect. As a result, the observed electrically driven magnetization switching is highly reliable, independent of the shape and size of the microstructures. This is a key factor that makes the studied multiferroic system very promising for integration in real-world magnetoelectric devices.

DOI: 10.1103/PhysRevMaterials.2.091402

New generation magnetic memory and logic devices are expected to merge high thermal stability and operational reliability with low-power consumption [1]. At the moment, magnetic memories are based on the manipulation of magnetization by electric currents [2], resulting in high-energy consumption. Accordingly, a new paradigm based on the control of magnetization by an electric field is highly desirable [3,4]. Multiferroic systems [5,6], where both the ferromagnetic and the ferroelectric order parameters are present and coupled to each other, have been extensively investigated for this scope. In particular, heterostructures consisting of a ferromagnetic thin film deposited on top of a $BaTiO_3$ ferroelectric/ferroelastic substrate have been reported to be a particularly interesting magnetoelectric system [7–15], where a strong magnetoelectric coupling at the interface between the two materials dominates the magnetic state in the ferromagnet. The very stable one-to-one correspondence between the ferroelectric (FE) and ferromagnetic (FM) domain patterns observed in some of those systems [7–9,16], joined with the naturally occurring micrometer size of those domains, opens up to a fully deterministic control of magnetism by electric fields at the micro- and nanoscale. This approach is potentially much more reliable if compared with what is obtained with other multiferroic heterostructures [17–20], where the strain-based magnetization manipulation can be strongly influenced by uncontrolled nonuniformities in the local strain at the microscale. However, even if already shown in extended films, the feasibility of such an approach in micro- and nanostructures remains an open question. Indeed, some attempt to study the magnetoelectric behavior of $BaTiO_3$/ferromagnet microdevices has been carried on in the past, as in the work by Baldrati *et al.* [21]. However, the lateral size of those devices is in the order of 100 μm, which is not small enough for studying the electrical control of magnetization at the micrometer and submicrometer scale, where ferromagnetic single domain structures start to emerge.

Here, we report electric-field-controlled magnetic domain wall (DW) motion and magnetization switching in $Co_{50}Fe_{50}$ micro- and submicrostructures on top of a $BaTiO_3$ single-crystal substrate. By x-ray microscopy we image both the FE state at the top surface of the $BaTiO_3$ substrate and the FM state of the magnetic structures patterned on top of the single crystal. In addition, the electrically induced magnetoelastic anisotropy is characterized by magneto-optic Kerr effect magnetometry. The results reported here are of great interest for the development of energy efficient magnetoelectric devices.

The studied multiferroic system consists of 20 nm-thick $Co_{50}Fe_{50}$ microstructures on top of a 500-μm-thick ferroelectric $BaTiO_3$ (BTO) single crystal (SurfaceNet GmbH, 48432 Rheine, Germany) as in Figs. 1(a) and 1(b). The ferroelectric substrate is in its tetragonal phase, with the polar axis lying in the plane of the crystal and initially in a ferroelectric a_1-a_2 multidomain state [7,22] [stripelike domains in Fig. 1(b)]. 90°-type FE domain walls (DWs) separate the a_1 from the a_2 domains [Fig. 1(c)]. The BTO crystal has a continuous Au bottom electrode and a Pt top electrode surrounding the patterned magnetic structures. The $Co_{50}Fe_{50}$ (CoFe) structure array includes squares and disks, with lateral sizes of 5 μm, 2 μm, 1 μm, and 500 nm. The magnetic structure patterning involves electron-beam lithography, magnetron-sputtering deposition, and lift-off techniques. Finally, a 1.5-nm-thick Pt layer is deposited over the top surface of the sample. The FE state of the BTO and the FM state of the CoFe structures are imaged respectively by exploiting the x-ray linear dichroism

*rloconte@berkeley.edu

†Corresponding author: jbokor@berkeley.edu

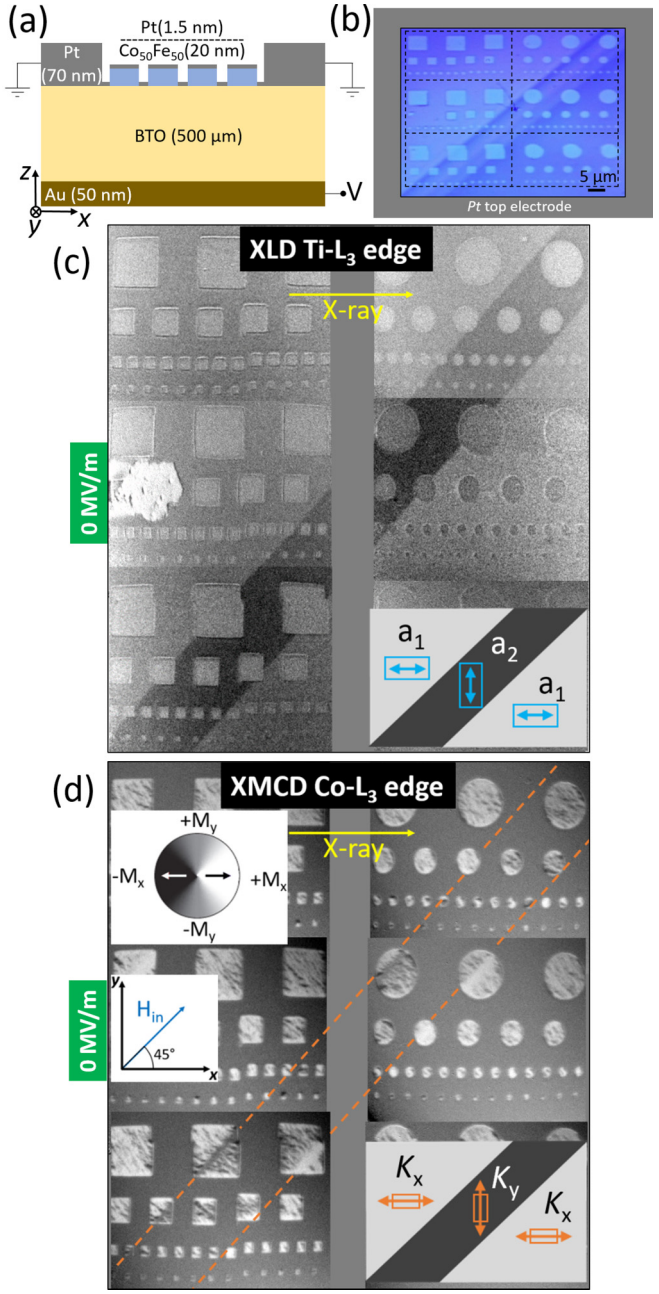

FIG. 1. (a) Sample schematic. (b) Optical microscopy image of the magnetic microstructures. Surrounding the microstructures is the Pt top electrode. (c) Aggregate of XLD-PEEM images showing the initial FE state of the sample in the ROI (FE polarization state described in the inset). (d) Aggregate of XMCD-PEEM images showing the initial FM state. Dashed lines indicate the position of the two FE DWs. The low inset describes the found magnetic anisotropy after deposition. The grayscale wheel describes the magnetic contrast. The blue arrow indicates the initializing magnetic field, $\mu_0 H_{in} = 250\,\mathrm{mT}$.

(XLD) at the Ti L_3 edge [23] and the x-ray magnetic circular dichroism (XMCD) at the Co L_3 edge [24], with a photoemission electron microscope (PEEM).

The initial FE state at the top surface of the BTO crystal in the region of interest (ROI) is shown in Fig. 1(c). Three different domains are visible, with the central domain (dark gray) having a different polarization state than the others (light gray). Initially, an external magnetic field ($\mu_0 H_{in} = 250\,\mathrm{mT}$) is applied along the 45° direction and then removed in order to initialize the magnetic structures. The resulting FM state of the CoFe structures is reported in Fig. 1(d). Most of the magnets are found to be magnetized along the positive x direction (white contrast). However, the magnetic structures lying on top of the central FE domain are found to be in a different state. Indeed, as recognizable in the magnetic structures located on top of the FE DWs [dashed orange lines in Fig. 1(d)], the parts of them lying on the central domain are mostly gray (magnetization$\|y$ axis), while the parts lying in the lateral domains are white (magnetization$\|x$ axis). This is in agreement with what reported in the literature [7,16], where a similar one-to-one FE-FM connection was observed for thin films. This is a magnetoelastic effect, where the magnetization inside the FM thin film aligns with the polar axis of the FE domains. Accordingly, we can conclude that the FE state in Fig. 1(c) is due to the presence of an a_1-a_2-a_1 domain pattern [inset in Fig. 1(c)], which generates a K_X-K_Y-K_X magnetoelastic anisotropy pattern for the CoFe magnets [inset in Fig. 1(d)].

After characterizing the electrically virgin sample, an electric field is applied *in situ* between the top and the bottom electrode. When a dc electric field $E = 0.6\,\mathrm{MV/m}$ is applied, a lateral displacement of the central a_2 FE domain is observed. The new state of the crystal is shown in Fig. 2(a), where the red arrows indicate the electrically driven displacement of the DWs. As described in Fig. 2(a), on the left, the polarization in the BTO crystal rotates from a_2 to a_1, while on the right, the rotation is from a_1 to a_2. A possible way to interpret the observed FE DW motion is based on the interaction between a new electrically nucleated out-of-plane domain (c domain) and the initial in-plane domains (a domains). Indeed, it has been reported that during the poling process of a tetragonal ferroelectric, new FE domains are nucleated and the propagation of those new ferroelectric domains can be stopped by ferroelastic domains initially present in the crystal, with their polarization being normal to the applied electric field [25,26]. Accordingly, the observed displacement of the central domain can be interpreted as the repulsion between such a domain and a newly nucleated ferroelectric domain underneath. However, due to the surface-sensitive nature of PEEM, we are unable to verify the actual presence of new FE c domains nucleated in the bulk of the BTO crystal. Finally, as visible in the magnetic image in Fig. 2(b), the 90° rotation of the electrical polarization in the BTO corresponds to a 90° rotation of the magnetization in the CoFe structures affected by the DW motion, testifying to a very effective electrical modification of the magnetic anisotropy. On the left (right), the magnetic easy axis is rotated from y to x (x to y). The magnetization rotation is in general nonuniform, resulting in the generation of a reoriented magnetic multidomain state [black-white contrast in Fig. 2(b)] in most of the affected magnetic structures.

From a technological point of view, it is very interesting to study the influence of the magnets' shape and size on the electrically controlled magnetic reorientation. Based on what is shown in Fig. 2(b), the size of the magnetic squares does not affect the ability to switch their magnetization. Indeed, every magnet located on top of the displaced DWs is reoriented, independently of its lateral size (5 µm–500 nm).

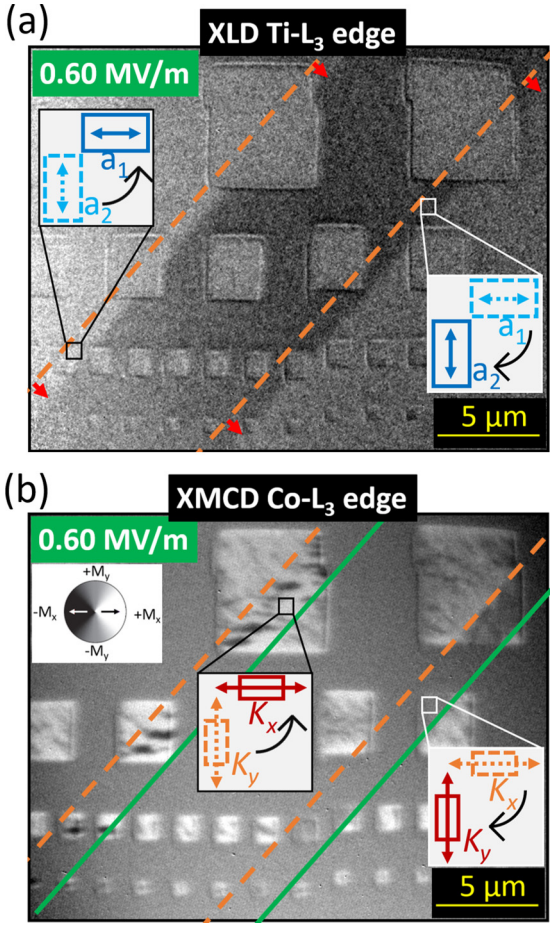

FIG. 2. (a) FE state at the bottom-left corner of the ROI with $E = 0.6\,\mathrm{MV/m}$. The red arrows indicate the electrically induced FE DW displacement. Insets describe the reorientation of the polar axis. (b) Corresponding FM state. The dashed orange and solid green lines delimit the areas where a magnetization is rotated. Insets describe the magnetic easy-axis rotation.

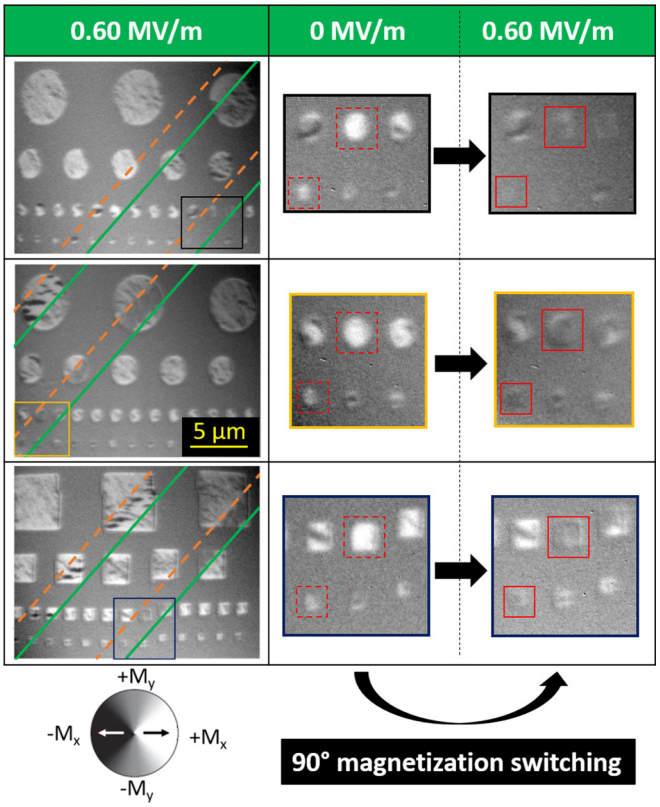

FIG. 3. The left column shows the magnetic state in three areas of the ROI, with $E = 0.6\,\mathrm{MV/m}$. The black, yellow, and blue solid frames indicate the regions enlarged in the right column, which report the magnetic state of 1-µm and 500-nm magnets at $E = 0\,\mathrm{MV/m}$ (left) and $0.6\,\mathrm{MV/m}$ (right). The dashed and the solid red frames indicate the initial and the final state of the highlighted nanomagnets, respectively.

Furthermore, the left column in Fig. 3 shows the electrically induced magnetic state of three different areas of the ROI. The magnetization reorientation happens in the squares as well as in the disks, independently of the shape. The right column in Fig. 3 shows in more detail the reorientation process in some of the small magnets, with a lateral size of 1 µm and 500 nm. At these lateral sizes some of the magnets are observed to be in an initial single domain state (white domain, dashed red frames). When the electric field is applied, the magnetization in those same magnets is switched to the y axis (gray domain, solid red frames). This demonstrates an electrically induced single-spin-like 90° magnetization switching, which is a key result in the applicability of such a material system in a hypothetical magnetoelectric memory device, where *white* (or *black*) and *gray* would represent the digital *1* and *0* states of a memory bit.

Based on the magnetization switching effect described above, we can calculate a converse magnetoelectric coupling coefficient (CMC) $\alpha_{\mathrm{CME}} = \mu_0 \Delta M/\Delta E = 2.7\times10^{-6}\,\mathrm{s/m}$, where ΔM is the induced change in magnetization ($M_S = 1.3\times10^6\,\mathrm{A/m}$, measured by vibrating sample magnetometry on a reference film on Si) and ΔE is the required electric field to induce such a magnetization change. This value is in line with the highest CMCs reported so far [7,27], highlighting the outstanding magnetoelectric properties of the studied multiferroic microstructures.

Finally, we study the magnetic state of the CoFe structures after further electrically poling the BTO crystal along the out-of-plane direction, so to directly quantify the electrically induced magnetic anisotropy in the CoFe structures. A single FE domain is observed for $E \geqslant 0.64\,\mathrm{MV/m}$ [polarization pointing *up*; see sample schematic in Fig. 1(a)] everywhere in the ROI, which is retained after removing the electric field. The corresponding magnetization state of the CoFe structures is shown in Fig. 4(a). All the magnetic parts lying on the original position of the central a_2 domain are now magnetized along x (light gray), while the rest of the structures are magnetized along y (dark gray). This is in agreement with what is reported in the literature [7], where the compressive strain generated along x (y) during the $a_1 \rightarrow c(a_2 \rightarrow c)$ transition in the FE state induces a magnetoelastic anisotropy pattern inside the ferromagnetic layer that is one-to-one connected to the initial a_1-a_2 multidomain state.

Magneto-optic Kerr effect (MOKE) magnetometry (using a Kerr microscope) is employed in order to quantify the final magnetic anisotropy inside the CoFe structures. Longitudinal-MOKE hysteresis loops are acquired, with a

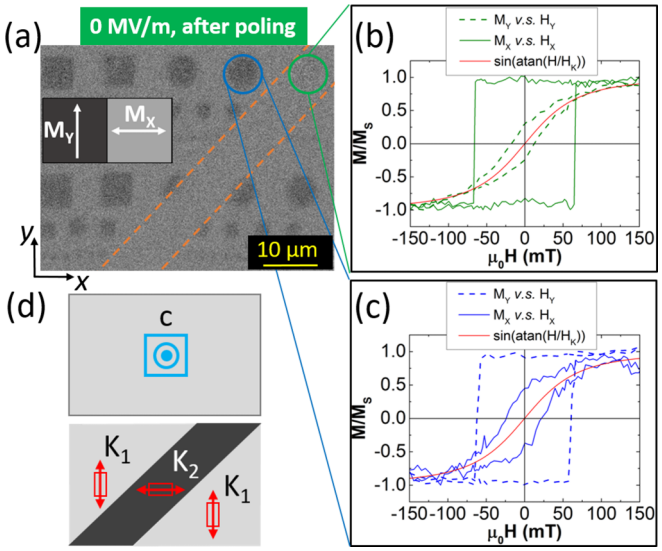

FIG. 4. (a) Differential wide field Kerr microscopy image of the sample with electrically poled substrate. The image is taken at zero magnetic field, after the sample is saturated by a field $\mu_0 H_y = 150\,\text{mT}$ along the y axis. (b) Longitudinal-MOKE hysteresis loops for the top-right disk with a magnetic field swept along x (solid line) and y (dashed line). (c) Same as in (b) for the top-center disk. (d) Schematic of the final FE state in the ROI and the induced magnetic anisotropy pattern.

magnetic field applied along the x and y, for the two 5-μm magnetic disks at the top-right corner of Fig. 4(a). As shown in Fig. 4(b), the top-right dot is characterized by a magnetic easy axis along x (M_x vs H_x, solid line), with a coercive field $\mu_0 H_c = 66\,\text{mT}$, while the magnetic hard axis is along y (M_y vs H_y, dashed line). The opposite situation is found for the top-center disk [see Fig. 4(c)]: The magnetic easy axis is along y (M_y vs H_y, dashed line), with a coercive field $\mu_0 H_c = 62\,\text{mT}$, and the magnetic hard axis is along x (M_x vs H_x, solid line). Based on this, we can assert that three different regions in the FM array correspond to a single c domain in the BTO crystal, with induced magnetic uniaxial anisotropy along $y(K_1)$ and $x(K_2)$ [see Fig. 4(d)]. The hard-axis anisotropy field H_K is extracted by fitting the plots in Figs. 4(b) and 4(c) with the following function, $\sin[\arctan(H/H_K)]$, where H is the applied magnetic field along the hard axis. An anisotropy field $\mu_0 H_K = 72 \pm 2\,\text{mT}$ ($74 \pm 4\,\text{mT}$) is extracted for the top-right (top-center) magnetic disk. We can calculate the induced magnetoelastic anisotropy as $K = \mu_0 M_S H_K/2$, so that the values $K_1 = 47 \pm 1\,\text{kJ/m}^3$ and $K_2 = 48 \pm 3\,\text{kJ/m}^3$ are extracted.

The theoretically expected maximum magnetoelastic anisotropy due to the $a \rightarrow c$ ferroelectric transformation is given by $K_{\text{m.e.}} = -3\lambda_s \varepsilon Y/2$; λ_s and Y are respectively the saturation magnetostriction coefficient and the Young's modulus of polycrystalline thin film $Co_{50}Fe_{50}$, while $\varepsilon = -1.1\%$ is the uniaxial compressive strain induced by the full $a \rightarrow c$ transformation in the BTO crystal ($a = 0.3992\,\text{nm}$, $c = 0.4036\,\text{nm}$) [7]. Based on the values available in the literature [28–31], we obtain $K_{\text{m.e.}} = 218\,\text{kJ/m}^3$ ($\lambda_s = 60\,\text{ppm}$ and $Y = 220\,\text{GPa}$), which is about four times bigger than the experimentally extracted values above. This seems to be in agreement with what is observed for similar CoFe thin films, where experimental values smaller than 50% of the theoretical maximum value were reported [7]. In part this can be attributed to an inefficient transfer of the strain from the substrate to magnetic layer [32]. In addition, the specific crystallographic configuration of the magnetic thin film in our microstructures can also play a role [31,33]. However, an in-depth understanding of this discrepancy is not the scope of this work and we leave this open question to a future study. Nevertheless, we are able to observe a full electrical switching of the magnetization in the magnetic microstructures, which is the main finding and a key result from an application point of view.

Finally, it is worth noting that in the last years the growth and electrical manipulation of $BaTiO_3$ thin films has been extensively studied [21,34–37], making this ferroelectric material compatible for heterogeneous integration on silicon electronics. On the other hand, the electrical control of the ferroelectric/ferromagnetic domain patter at the micrometer scale in thin-film $BaTiO_3$/FM systems is yet to be proven, calling for further developments. Accordingly, once the FE DW-driven magnetization switching reported here will be demonstrated in systems with thin-film BTO as well, BTO/CoFe multiferroic nanostructures are expected to become a concrete option for the design of real-world magnetoelectric memory devices.

In summary, an electric-field-controlled magnetic DW motion and magnetization switching are achieved in $Co_{50}Fe_{50}$ micro- and submicrostructures on top of a $BaTiO_3$ single crystal. The initial ferromagnetic state of the CoFe structures is defined by the ferroelectric domain patter present in the BTO crystal. The subsequent electrical poling of the substrate induces a motion of the ferroelectric DWs, which drives magnetic DWs to move, generating a 90° rotation of the magnetization in the structures. An electrically induced single-spin-like magnetization switching is observed in the 1-μm and 500-nm structures which were initially found in a single domain state. Finally, a giant converse magnetoelectric coefficient, $\alpha_{\text{CME}} = 2.7 \times 10^{-6}\,\text{s/m}$, is extracted, which is among the highest reported so far. All this demonstrates the high reliability and efficiency of the studied BTO/CoFe microstructures, which are found to be a promising candidate for the development of new, low-power magnetoelectric memory devices. This work is expected to motivate more experimental and theoretical studies focused on magnetic nanostructures on top of BTO single crystals and epitaxial thin films.

Note added in proof. Recently, we became aware of a relevant study by Ghidini and colleagues [38], which focuses on the investigation of the electrical control of magnetism in Ni microdots on a $BaTiO_3$ single crystal.

We gratefully acknowledge support from the National Science Foundation (NSF) through the Cooperative Agreement Award EEC-1160504 for Solicitation NSF 11-537 (TANMS) and the NSF Center for Energy Efficient Electronics Science (supporting the sample preparation). The work at the Advanced Light Source at Lawrence Berkeley National Laboratory (XMCD-PEEM at beamline 11.0.1) is supported by the Director, Office of Science, Office of Basic Energy Sciences, U.S. Department of Energy, under

Contract No. DE-AC02-05CH11231. This work was also supported by the Director, Office of Science, Office of Basic Energy Sciences, Materials Sciences and Engineering Division, of the U.S. Department of Energy under Contract No. DE-AC02-05-CH11231 within the Nonequilibrium Magnetic Materials Program (MSMAG) (supporting the PEEM experiment). Finally, we acknowledge the support by the ANR PIAF Project No. ANR17-CE09-0030-03 of the French Agence Nationale de la Recherche (supporting the MOKE experiment).

[1] S. Manipatruni, D. E. Nikonov, R. Ramesh, H. Li, and I. A. Young, arXiv:1512.05428.
[2] K. L. Wang, J. G. Alzate, and P. Khalili Amiri, J. Phys. D: Appl. Phys. **46**, 074003 (2013).
[3] V. Novosad, Y. Otani, A. Ohsawa, S. G. Kim, K. Fukamichi, J. Koike, K. Maruyama, O. Kitakami, and Y. Shimada, J. Appl. Phys. **87**, 6400 (2000).
[4] M. Bibes and A. Barthélémy, Nat. Mater. **7**, 425 (2008).
[5] R. Ramesh and N. A. Spaldin, Nat. Mater. **6**, 21 (2007).
[6] W. Eerenstein, N. D. Mathur, and J. F. Scott, Nature (London) **442**, 759 (2006).
[7] T. H. E. Lahtinen, K. J. A. Franke, and S. van Dijken, Sci. Rep. **2**, 1 (2012).
[8] T. H. E. Lahtinen, J. O. Tuomi, and S. Van Dijken, Adv. Mater. **23**, 3187 (2011).
[9] K. J. A. Franke, B. Van de Wiele, Y. Shirahata, S. J. Hämälainen, T. Taniyama, and S. van Dijken, Phys. Rev. X **5**, 011010 (2015).
[10] S. Brivio, D. Petti, R. Bertacco, and J. C. Cezar, Appl. Phys. Lett. **98**, 092505 (2011).
[11] M. Ghidini, F. Maccherozzi, X. Moya, L. C. Phillips, W. Yan, J. Soussi, N. Métallier, M. E. Vickers, N. J. Steinke, R. Mansell, C. H. W. Barnes, S. S. Dhesi, and N. D. Mathur, Adv. Mater. **27**, 1460 (2015).
[12] L. C. Phillips, R. O. Cherifi, V. Ivanovskaya, A. Zobelli, I. C. Infante, E. Jacquet, N. Guiblin, A. A. Ünal, F. Kronast, B. Dkhil, A. Barthélémy, M. Bibes, and S. Valencia, Sci. Rep. **5**, 10026 (2015).
[13] R. O. Cherifi, V. Ivanovskaya, L. C. Phillips, A. Zobelli, I. C. Infante, E. Jacquet, V. Garcia, S. Fusil, P. R. Briddon, N. Guiblin, A. Mougin, A. A. Ünal, F. Kronast, S. Valencia, B. Dkhil, A. Barthélémy, and M. Bibes, Nat. Mater. **13**, 345 (2014).
[14] O. Rousseau, R. Weil, S. Rohart, and A. Mougin, Sci. Rep. **6**, 23038 (2016).
[15] R. V Chopdekar, V. K. Malik, A. F. Rodríguez, L. Le Guyader, Y. Takamura, A. Scholl, D. Stender, C. W. Schneider, C. Bernhard, F. Nolting, and L. J. Heyderman, Phys. Rev. B **86**, 014408 (2012).
[16] T. H. E. Lahtinen, J. O. Tuomi, and S. Van Dijken, IEEE Trans. Magn. **47**, 3768 (2011).
[17] M. Buzzi, R. V. Chopdekar, J. L. Hockel, A. Bur, T. Wu, N. Pilet, P. Warnicke, G. P. Carman, L. J. Heyderman, and F. Nolting, Phys. Rev. Lett. **111**, 027204 (2013).
[18] J. T. Heron, J. L. Bosse, Q. He, Y. Gao, M. Trassin, L. Ye, J. D. Clarkson, C. Wang, J. Liu, S. Salahuddin, D. C. Ralph, D. G. Schlom, J. Íñiguez, B. D. Huey, and R. Ramesh, Nature (London) **516**, 370 (2014).
[19] H. Sohn, M. E. Nowakowski, C. Y. Liang, J. L. Hockel, K. Wetzlar, S. Keller, B. M. McLellan, M. A. Marcus, A. Doran, A. Young, M. Kläui, G. P. Carman, J. Bokor, and R. N. Candler, ACS Nano **9**, 4814 (2015).
[20] R. Lo Conte, Z. Xiao, C. Chen, C. V Stan, J. Gorchon, A. El-Ghazaly, M. E. Nowakowski, H. Sohn, A. Pattabi, A. Scholl, N. Tamura, A. Sepulveda, G. P. Carman, R. N. Candler, and J. Bokor, Nano Lett. **18**, 1952 (2018).
[21] L. Baldrati, C. Rinaldi, A. Manuzzi, M. Asa, L. Aballe, M. Foerster, N. Biškup, M. Varela, M. Cantoni, and R. Bertacco, Adv. Electron. Mater. **2**, 1600085 (2016).
[22] A. F. Devonshire, London, Edinburgh Dublin Philos. Mag. J. Sci. **40**, 1040 (1949).
[23] E. Arenholz, G. van der Laan, A. Fraile-Rodríguez, P. Yu, Q. He, and R. Ramesh, Phys. Rev. B **82**, 140103(R) (2010).
[24] A. Scholl, *Reference Module in Materials Science and Materials Engineering* (Elsevier, Amsterdam, 2016).
[25] E. A. Little, Phys. Rev. **98**, 978 (1955).
[26] P. Gao, J. Britson, J. R. Jokisaari, C. T. Nelson, S.-H. Baek, Y. Wang, C.-B. Eom, L.-Q. Chen, and X. Pan, Nat. Commun. **4**, 2791 (2013).
[27] M. Staruch, D. B. Gopman, Y. L. Iunin, R. D. Shull, S. F. Cheng, K. Bussmann, and P. Finkel, Sci. Rep. **6**, 37429 (2016).
[28] L. C. Wang, H. J. Hatton, M. D. Cooke, M. R. J. Gibbs, W. M. Rainforth, and C. J. D. Hetherington, J. Appl. Phys. **89**, 7511 (2001).
[29] T. A. Lafford, M. R. J. Gibbs, and C. Shearwood, J. Magn. Magn. Mater. **132**, 89 (1994).
[30] D. Hunter, W. Osborn, K. Wang, N. Kazantseva, J. Hattrick-Simpers, R. Suchoski, R. Takahashi, M. L. Young, A. Mehta, L. A. Bendersky, S. E. Lofland, M. Wuttig, and I. Takeuchi, Nat. Commun. **2**, 518 (2011).
[31] M. D. Cooke, L.-C. Wang, R. Watts, R. Zuberek, G. Heydon, W. M. Rainforth, and G. A. Gehring, J. Phys. D: Appl. Phys. **33**, 1450 (2000).
[32] M. Feng, J.-J. Wang, J.-M. Hu, J. Wang, J. Ma, H.-B. Li, Y. Shen, Y.-H. Lin, L.-Q. Chen, and C.-W. Nan, Appl. Phys. Lett. **106**, 072901 (2015).
[33] H. S. Jung, W. D. Doyle, and S. Matsunuma, J. Appl. Phys. **93**, 6462 (2003).
[34] K. J. Choi, M. Biegalski, Y. L. Li, A. Sharan, J. Schubert, R. Uecker, P. Reiche, Y. B. Chen, X. Q. Pan, V. Gopalan, L.-Q. Chen, D. G. Schlom, and C. B. Eom, Science **306**, 1005 (2004).
[35] K. J. Kormondy, Y. Popoff, M. Sousa, F. Eltes, D. Caimi, M. D. Rossell, M. Fiebig, P. Hoffmann, C. Marchiori, M. Reinke, M. Trassin, A. A. Demkov, J. Fompeyrine, and S. Abel, Nanotechnology **28**, 075706 (2017).
[36] A. S. Everhardt, S. Matzen, N. Domingo, G. Catalan, and B. Noheda, Adv. Electron. Mater. **2**, 1500214 (2016).
[37] C. Dubourdieu, J. Bruley, T. M. Arruda, A. Posadas, J. Jordan-Sweet, M. M. Frank, E. Cartier, D. J. Frank, S. V. Kalinin, A. A. Demkov, and V. Narayanan, Nat. Nanotechnol. **8**, 748 (2013).
[38] M. Ghidini, B. Zhu, R. Mansell, R. Pellicelli, A. Lesaine, X. Moya, S. Crossley, B. Nair, F. Maccherozzi, C. H. W. Barnes, R. P. Cowburn, S. S. Dhesi, and N. D. Mathur, J. Phys. D: Appl. Phys. **51**, 224007 (2018).